

# PHYSICS-INFORMED DIFFUSION GENERATION FOR GEOMAGNETIC MAP INTERPOLATION

Wenda Li<sup>1</sup> Tongya Zheng<sup>2</sup> Kaixuan Chen<sup>1</sup> Shunyu Liu<sup>1</sup> Haoze Jiang<sup>1</sup>  
 Yunzhi Hao<sup>2</sup> Rui Miao<sup>3</sup> Zujie Ren<sup>3†</sup> Mingli Song<sup>1</sup> Hang Shi<sup>3</sup> Gang Chen<sup>1</sup>

<sup>1</sup> State Key Laboratory of Blockchain and Data Security, Zhejiang University

<sup>2</sup> High-Performance Intelligent Computing Research Center for Ultra-Large Scale Graph Data, School of Computer and Computing Science, Hangzhou City University

<sup>3</sup> Zhejiang Lab

## ABSTRACT

Geomagnetic map interpolation aims to infer unobserved geomagnetic data at spatial points, yielding critical applications in navigation and resource exploration. However, existing methods for scattered data interpolation are not specifically designed for geomagnetic maps, which inevitably leads to suboptimal performance due to detection noise and the laws of physics. Therefore, we propose a **Physics-informed Diffusion Generation** framework (PDG) to interpolate incomplete geomagnetic maps. First, we design a physics-informed mask strategy to guide the diffusion generation process based on a local receptive field, effectively eliminating noise interference. Second, we impose a physics-informed constraint on the diffusion generation results following the kriging principle of geomagnetic maps, ensuring strict adherence to the laws of physics. Extensive experiments and in-depth analyses on four real-world datasets demonstrate the superiority and effectiveness of each component of PDG.

**Index Terms**— Geomagnetic Map, Data Interpolation, Diffusion Model, Physics-informed Model

## 1. INTRODUCTION

Geomagnetic map interpolation [1, 2] aims to infer unobserved magnetic data in space and is widely applied in navigation [3], resource exploration [4], and precise positioning [5]. In practical measurements, environmental factors often cause the measurement trajectory to exhibit a chain-like distribution, and the collected data typically contain noise. Traditional methods [6, 7, 8] are based on the principle of local consistency [9, 10] in geomagnetic data, where the geomagnetic field varies smoothly and continuously across neighboring regions, estimating values at unobserved points using nearby observations and assigning spatial weights according to explicitly defined functional relationships. However, when

applied to large-scale datasets that often contain noise, these methods typically face challenges in model performance.

Recently, deep learning-based methods have emerged to capture latent correlations between observed and unobserved points for scattered data interpolation, which shares similar data formats with geomagnetic data. Neural Processes predict the distribution of target points from context data using conditional encoding [11], attention mechanisms [7], or bootstrapping [12] to estimate uncertainty. NIERT [13] adopts a pre-trained Transformer on synthetic functions to improve interpolation and generalization. HINT [14] hierarchically leverages observed-point residuals to iteratively refine interpolation with lightweight modules. Despite the effective spatial correlation modeling, the aforementioned methods are not particularly designed for geomagnetic map interpolation. Specifically, two challenges remain in scattered data interpolation in geomagnetic data. First, these methods typically consider clean data without accounting for noise, resulting in significant disturbances in geomagnetic data due to noise. Second, neural modules often disrupt physical smoothness and continuity because of their strong nonlinearity, thereby violating the laws of physics in the geomagnetic map.

To address the above challenges, we propose a **Physics-informed Diffusion Generation** for geomagnetic map interpolation (PDG). First, we introduce a **geomagnetic diffusion model** that interpolates geomagnetic data through a step-wise iterative generation process, effectively suppressing noise in the observations. To further reduce noise, we design a **physics-informed mask** strategy that dynamically adjusts the local receptive field during the diffusion process, guiding data generation with physical principles. To ensure adherence of the diffusion-generated results to physical principles, we incorporate a **physics-informed constraint** guided by the Kriging approach. Extensive experiments on four real-world geomagnetic datasets show that PDG reduces the interpolation error by up to 80%. Visualization analysis further illustrates its superiority in local areas, and comprehensive ablation studies verify the effectiveness of each component.

<sup>†</sup> Corresponding author: Zujie Ren (renzju@zju.edu.cn)

## 2. PRELIMINARY

**Geomagnetic Map Interpolation.** For a spatial coordinate  $m^i = (\text{lon}_i, \text{lat}_i)$ , the corresponding geomagnetic field intensity is  $x^i \in \mathbb{R}^d$ , measured in nanoteslas (nT). Geomagnetic map interpolation aims to predict the magnetic field intensity  $x^{ta}$  at a target location  $m^{ta}$ , given the coordinates  $m^o = \{m^1, \dots, m^n\}$  and magnetic field intensity measurements  $x^o = \{x^1, \dots, x^n\}$  of multiple observed points:

$$x^{ta} = f(m^o, x^o, m^{ta}), \quad (1)$$

where  $f(\cdot)$  denotes the interpolation function that estimates the field at an unknown location based on the observed data.

**Diffusion Models.** Diffusion models [15, 16] are probabilistic generative models rooted in principles of non-equilibrium thermodynamics and stochastic differential equations. A canonical example is the Denoising Diffusion Probabilistic Model (DDPM) [17], which comprises a forward process for noise injection and a reverse process for generating data from Gaussian noise. During the forward process, an initial input  $x_0 \sim q(x_0)$  is gradually corrupted into a Gaussian noise vector through  $t$  steps that can be described as a Markov chain:

$$q(x_t | x_{t-1}) = \mathcal{N} \left( \sqrt{1 - \beta_t} x_{t-1}, \beta_t I \right), \quad 1 \leq t \leq T, \quad (2)$$

where  $\beta_t \in [0, 1]$  represents the noise level at step  $t$ . Alternatively, the distribution of  $x_t$  conditioned directly on  $x_0$  can be written as  $q(x_t | x_0) = \mathcal{N} \left( x_t; \sqrt{\bar{\alpha}_t} x_0, (1 - \bar{\alpha}_t) I \right)$ , where  $\bar{\alpha}_t = \prod_{s=1}^t \alpha_s$  and  $\alpha_t = 1 - \beta_t$ . Thus,  $x_t$  can be simply obtained as

$$x_t = \sqrt{\bar{\alpha}_t} x_0 + \sqrt{1 - \bar{\alpha}_t} \epsilon, \quad (3)$$

where  $\epsilon$  is standard Gaussian noise. During the reverse process, a neural network model  $\epsilon_\theta$  is used to learn the denoising distribution  $p_\theta(x_{t-1} | x_t) = \mathcal{N} \left( x_{t-1}; \mu_\theta(x_t, t), \sigma_\theta(x_t, t) \right)$ , where the variance  $\sigma_\theta(x_t, t)$  is often fixed to  $\sigma^2 I$ , and the mean  $\mu_\theta(x_t, t)$  is computed as  $\mu_\theta(x_t, t) = \frac{1}{\sqrt{\alpha_t}} x_t - \frac{1 - \alpha_t}{\sqrt{1 - \bar{\alpha}_t} \sqrt{\alpha_t}} \epsilon_\theta(x_t, t)$ . The training objective is to minimize the following loss:

$$\mathcal{L}_\epsilon = \mathbb{E}_{t, x_0, \epsilon} \|\epsilon - \epsilon_\theta(x_t, t)\|_2^2. \quad (4)$$

## 3. METHOD

In this section, we introduce PDG, a novel physics-informed diffusion generation framework for geomagnetic map interpolation. The architecture of our method is shown in Figure 1.

### 3.1. Physics-Informed Geomagnetic Diffusion

Noise in measurement data, caused by environmental factors, affects the interpolation of geomagnetic maps. To reduce the impact of noise, we employ a diffusion model to reconstruct

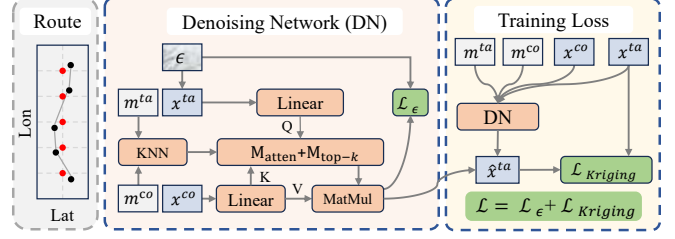


Fig. 1. The overall framework of PDG.

missing data through a step-by-step denoising process. Based on the physical principle of local consistency, we design a physics-informed mask strategy that dynamically adjusts the local neighborhood range at each diffusion step to suppress noise interference further while generating smooth data. A conditional diffusion model [18] is adopted to predict missing geomagnetic data, leveraging known observations as spatial cues to guide the prediction of missing values more accurately compared with an unconditional diffusion model that generates samples solely from noise.

Given the observed data pairs  $(m^o, x^o)$  and the target data pairs  $(m^{ta}, x^{ta})$ . The objective of the denoising model is to estimate the noise added to the magnetic field intensities  $x^{ta}$  at the target locations  $m^{ta}$ . At the specific diffusion step  $t$ , Gaussian noise  $\epsilon \sim \mathcal{N}(0, I)$  is added to the target magnetic field intensities to generate the noisy inputs as Equation 3:

$$x_t^{ta} = \sqrt{\bar{\alpha}_t} x_0^{ta} + \sqrt{1 - \bar{\alpha}_t} \epsilon, \quad (5)$$

where  $x_0^{ta}$  represents the true magnetic field intensities at  $m^{ta}$ . The observed data pairs  $(m^o, x^o)$ , which are used as conditions  $(m^{co}, x^{co})$ , are fed into the denoising model along with the noised target pairs  $(m^{ta}, x_t^{ta})$ . We first apply linear projections to the conditional pair  $(m^{co}, x^{co})$  and target pair  $(m^{ta}, x^{ta})$  to obtain their latent representations:  $h_t = \text{Linear}(m_t, x_t) + p^t$ , where  $p^t = \text{FFN}(\text{Emb}(t))$  and  $\text{Emb}(t) = (\sin(10^{\frac{4i}{w-1}} t))_{i=0}^{w-1} \parallel (\cos(10^{\frac{4i}{w-1}} t))_{i=0}^{w-1}$ . Here,  $\text{Linear}(\cdot)$  denotes a learnable linear projection layer,  $\text{FFN}(\cdot)$  refers to the Feedforward Neural Network,  $p^t$  is the diffusion step embedding at step  $t$ ,  $\text{Emb}(t)$  is a  $d$ -dimensional vector for step encoding, and  $w = d/2$ .

In the physics-informed mask, for each target point, the receptive field is restricted to the top- $k$  geographically closest conditional points, thereby reducing noise from points outside the receptive field and generating smooth data. Specifically,  $M_{\text{top-}k} = \mathbf{1}(m^{co} \in \text{KNN}(m^{ta}))$ . As the denoising process progresses, the model generates increasingly accurate data, so the receptive field of each target point is set as a function of the diffusion step, i.e.,  $k = K(t)$ . In the early stages, a larger  $K$  is used to incorporate more conditional points for coarse estimation, while a smaller  $K$  is applied in later stages to capture fine-grained local patterns. Specifically,  $K(t) = K_{\min} + \frac{t}{T} \times (K_{\max} - K_{\min})$ , where  $t$  is the current diffusion

timestep,  $T$  is the total number of diffusion steps,  $K_{\min}$  is the minimum neighborhood size used in the final stages of denoising, and  $K_{\max}$  is the maximum neighborhood size used in the initial stages.

A cross-attention mechanism is utilized to model the spatial dependencies between target points and available conditional points. First, we obtain the query, key, and value vectors through linear projections where  $Q = h_t^{ta}W^Q$ ,  $K = h_t^{co}W^K$ , and  $V = h_t^{co}W^V$ .

$$o_t^{ta} = \text{Softmax} \left( \frac{QK^\top}{\sqrt{D}} \odot M_{\text{top}-k} \right) V, \quad (6)$$

where  $\text{Softmax}(\cdot)$  normalizes the input scores into a probability distribution,  $W^Q$ ,  $W^K$ , and  $W^V$  are learnable weight matrices for the query, key, and value projections,  $D$  is the dimensionality of the query and key vectors, used for scaling. Then, the predicted noise  $\hat{\epsilon}_t^{ta}$  is obtained via a residual connection and an MLP, i.e.,  $\hat{\epsilon}_t^{ta} = \text{MLP}(h_t^{ta} + o_t^{ta})$ . At diffusion step  $t$ , the denoised magnetic field intensities  $\hat{x}_0^{ta}$  is recovered using the standard DDPM reverse formulation:

$$\hat{x}_0^{ta} = \frac{x_0^{ta} - \sqrt{1 - \bar{\alpha}_t} \cdot \hat{\epsilon}_t^{ta}}{\sqrt{\bar{\alpha}_t}}. \quad (7)$$

### 3.2. Kriging-Guided Physics-Informed Constraint

To enhance the physical consistency of predictions, we introduce a kriging-guided physics-informed loss. This loss draws on the principle of kriging to model spatial autocorrelation [6], using the similarity of nearby points to constrain the neural network outputs to reflect the spatial variations observed in the real geomagnetic field. For any pair of locations  $i$  and  $j$ , we define the empirical variogram based on the ground truth and predicted values as  $\gamma_{\text{true}}(r^{ij}) = \frac{1}{2}(x^{ta,i} - x^{ta,j})^2$  and  $\gamma_{\text{pred}}(r^{ij}) = \frac{1}{2}(\hat{x}^{ta,i} - \hat{x}^{ta,j})^2$ , where  $r_{ij} = |m^{ta,i} - m^{ta,j}|$  denotes the Euclidean distance between the target locations  $m^{ta,i}$  and  $m^{ta,j}$ .

To capture local spatial structures while maintaining computational efficiency, for each target location  $i$ , we select its  $t$  nearest neighbors, denoted as  $\mathcal{N}_t(i)$ . The kriging-guided physics-informed loss is then formulated as:

$$\mathcal{L}_{\text{Kriging}} = \frac{1}{|m^{ta}|} \sum_{i=1}^{|m^{ta}|} \frac{1}{t} \sum_{j \in \mathcal{N}_t(i)} (\gamma_{\text{pred}}(r^{ij}) - \gamma_{\text{true}}(r^{ij}))^2, \quad (8)$$

where  $|m^{ta}|$  is the number of target locations.

### 3.3. Training Process

During the training process, the denoising loss at diffusion step  $t$  is defined as the mean squared error between the true noise and the predicted noise. During training, the denoising loss at diffusion step  $t$  is defined as the mean squared error between the true noise and the predicted noise, i.e.,  $\mathcal{L}_\epsilon =$

$\mathbb{E}_{x_t^{ta}, t, \epsilon \sim \mathcal{N}(0, 1)} [\|\epsilon - \epsilon_\theta(x_t, t)\|^2]$ . Together with the kriging-guided physics-informed loss,  $\mathcal{L}_{\text{Kriging}}$ , the total loss  $\mathcal{L}$  is

$$\mathcal{L} = \mathcal{L}_\epsilon + \lambda \mathcal{L}_{\text{Kriging}}. \quad (9)$$

where  $\lambda$  is a weighted coefficient.

## 4. EXPERIMENTS

### 4.1. Experiment Settings

**Datasets.** We collected geomagnetic data along UAV flight paths in the city A<sup>1</sup> and city B<sup>1</sup> regions. For city A, datasets A-InX, A-InZ, and A-OutZ are constructed from *in-cabin* components X and Z and the *out-of-cabin* Z component, respectively. For city B, dataset B-InT is based on the *in-cabin* total field intensity T. All datasets are split into training, validation, and test sets in an 8:1:1 ratio. All experiments were performed using an NVIDIA A800 GPU.

**Baselines.** To evaluate the interpolation accuracy, we compared PDG with existing representative neural network-based interpolation methods, including Conditional Neural Processes (CNP) [11], Attentive Neural Processes (ANP) [19], Bootstrapping Attentive Neural Processes (BANP) [12], NIERT [13], TFR-Transformer [20], and HINT [14].

### 4.2. Results

**Quantitative Results.** Table 1 shows that PDG reduces interpolation error by 80% on average across four real-world datasets, while other deep-learning methods perform much worse with errors several times larger. Although HINT achieves comparable performance on the A-InX dataset, it underperforms on the remaining datasets and suffers from out-of-memory (OOM) issues, underscoring the necessity of our framework for both accurate and efficient geomagnetic interpolation.

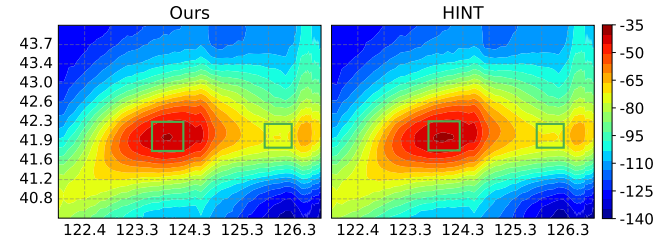


**Fig. 2.** High-precision geomagnetic map of dataset A-OutZ. The x-axis denotes longitude, and the y-axis denotes latitude.

**Qualitative Results.** Figure 2 shows that our method and the baseline HINT both capture the large-scale geomagnetic distribution well, exhibiting consistent patterns in major

<sup>1</sup>To preserve confidentiality, the identities of the two cities analyzed in this study are anonymized and represented by abbreviations.

**Table 1.** Overall performance comparison, with the best result on each dataset highlighted in **bold**. “OOM” stands for “Out of Memory”.

Dataset	Metric	CNP	BANP	ANP	TFR	Niert	HINT	PDG
A-InX	RMSE	2.511	2.363	2.696	2.135	1.320	0.560	<b>0.552</b>
	MAE	2.511	2.064	2.362	1.866	1.085	0.449	<b>0.422</b>
	MAPE	0.783	2.064	0.947	0.636	0.357	0.449	<b>0.144</b>
	MSE	7.942	7.187	10.089	6.647	1.965	0.341	<b>0.332</b>
A-InZ	RMSE	2.038	1.931	5.657	1.595	2.650	0.886	<b>0.719</b>
	MAE	1.734	1.592	4.636	1.388	2.155	0.665	<b>0.556</b>
	MAPE	0.696	1.592	1.900	0.411	0.603	0.170	<b>0.132</b>
	MSE	4.592	4.184	47.590	3.080	7.689	0.917	<b>0.540</b>
B-InT	RMSE	23.355	OOD	43.260	44.637	31.811	OOD	<b>1.092</b>
	MAE	18.781	OOD	35.492	34.931	24.613	OOD	<b>0.511</b>
	MAPE	0.573	OOD	0.840	1.161	0.964	OOD	<b>0.013</b>
	MSE	635.520	OOD	1982.100	2162.436	1099.566	OOD	<b>7.997</b>
A-OutZ	RMSE	2.189	2.525	3.508	2.217	1.340	0.564	<b>0.288</b>
	MAE	1.863	2.200	3.069	1.952	1.083	0.470	<b>0.227</b>
	MAPE	0.554	0.661	1.188	0.617	0.238	0.173	<b>0.064</b>
	MSE	5.686	8.360	16.642	6.131	2.215	0.337	<b>0.120</b>

**Table 2.** Ablation study on PDG. “PIM” and “PIC” stand for physics-informed mask and kriging-guided physics-informed loss, respectively.

Methods	A-InX		A-InZ		B-InT		A-OutZ	
	RMSE	MAPE	RMSE	MAPE	RMSE	MAPE	RMSE	MAPE
w/o PIM	0.609	0.145	0.896	0.140	2.019	0.032	0.348	0.071
w/o PIC	0.631	0.155	0.913	0.146	2.020	0.025	0.337	0.064
PDG	<b>0.552</b>	<b>0.144</b>	<b>0.719</b>	<b>0.132</b>	<b>1.092</b>	<b>0.013</b>	<b>0.288</b>	<b>0.064</b>

anomaly regions such as the central high-value zone. However, in local areas, our method performs better: the contour lines are smoother with more natural transitions, effectively suppressing noise. In contrast, HINT shows fluctuations and spikes, with abrupt high or low values near certain points, indicating higher sensitivity to outliers. Overall, our method is more robust and produces more realistic and reliable geomagnetic maps.

**Ablation Study of Different Components.** To more thoroughly evaluate PDG, we conducted ablation studies by removing key components. As shown in Table 2, removing either the physics-informed mask or the kriging-guided physics-informed loss degrades performance, indicating that both noise handling and adherence to local physical consistency are crucial for improving interpolation accuracy in geomagnetic map interpolation tasks.

**Parameter Sensitivity Study on Sampling Steps.** We conducted a parameter sensitivity experiment to investigate the impact of sampling steps. Six sampling steps were selected: 5, 10, 20, 30, 40, and 50. As shown in Table 3, setting the sampling steps within the range of 5–20 achieves a good balance between performance and efficiency. This indicates that excessively large sampling steps do not necessarily improve accuracy but instead increase computational overhead, whereas moderate sampling steps can provide a better trade-off between accuracy and efficiency.

**Parameter Sensitivity Study on  $K_{\max}$  and  $K_{\min}$ .** We analyzed the impact of different values of  $K_{\max}$  and  $K_{\min}$  on

**Table 3.** Parameter sensitivity study on sampling steps.

step	A-InX		A-InZ		B-InT		A-OutZ	
	RMSE	MAPE	RMSE	MAPE	RMSE	MAPE	RMSE	MAPE
5	0.492	0.143	0.636	0.122	0.998	0.014	0.366	0.074
10	0.552	0.144	0.719	0.132	1.092	0.013	0.282	0.064
20	0.555	0.150	0.690	0.138	1.044	0.014	0.282	0.068
30	0.571	0.150	0.725	0.140	1.013	0.013	0.285	0.072
40	0.575	0.146	0.733	0.144	1.094	0.014	0.287	0.080
50	0.577	0.153	0.748	0.147	1.033	0.014	0.290	0.066

**Table 4.** Parameter sensitivity study on  $K_{\max}$  and  $K_{\min}$ .

$K_{\max}$	$K_{\min}$	A-InX		A-InZ		B-InT		A-OutZ	
		RMSE	MAPE	RMSE	MAPE	RMSE	MAPE	RMSE	MAPE
1500	32	0.561	0.141	0.864	0.142	1.901	0.016	0.307	0.064
	64	0.562	0.142	0.866	0.143	1.945	0.016	0.308	0.064
1000	32	<b>0.552</b>	<b>0.141</b>	0.724	0.137	<b>1.092</b>	<b>0.013</b>	<b>0.288</b>	<b>0.062</b>
	64	0.552	0.141	0.727	0.138	1.132	0.013	0.289	0.063
500	32	0.554	0.143	<b>0.719</b>	<b>0.132</b>	1.129	0.018	0.302	0.059
	64	0.555	0.143	0.719	0.132	1.171	0.019	0.303	0.060

the interpolation performance. Table 4 shows that  $K_{\max}$  has a significant effect on the completion results. This is because, during the initial steps, the neighborhood size is large and the geomagnetic data exhibits strong fluctuations. Selecting an appropriate range is crucial for capturing the overall spatial patterns and ensuring accurate interpolation. In contrast,  $K_{\min}$  has a relatively minor impact on the final results. As the number of steps decreases, the neighborhood size becomes smaller and the geomagnetic fluctuations are limited, meaning the model primarily serves to refine and consolidate the interpolation results rather than improve them substantially.

## 5. CONCLUSION

In this paper, we propose PDG, a physics-informed diffusion generation framework for geomagnetic map interpolation. By integrating a geomagnetic diffusion model, a physics-informed mask, and physical constraints, our method effectively suppresses noise and enforces physical consistency. Experiments on four real-world datasets show up to 80% error reduction and superior performance in irregular regions, while ablation and visualization studies further demonstrate the effectiveness and advantages of each component.

**Relation to Prior Work.** The work presented here focuses on the development of a geomagnetic data interpolation algorithm that accounts for both noise suppression and compliance with physical principles. In contrast, the work by Shizhe and Dongbo [14] reduces interpolation errors through a hierarchical residual optimization method. While the present study is related to recent scattered data interpolation methods [12, 13, 14], it is specifically designed for geomagnetic data and effectively exploits geomagnetic characteristics that were not addressed in earlier studies.

## 6. ACKNOWLEDGEMENTS

This work was supported by the National Natural Science Foundation of China (Grant No. 62506330), the Zhejiang Provincial Natural Science Foundation of China (Grant No. LQN26F020007), Zhejiang Province High-Level Talents Special Support Program "Leading Talent of Technological Innovation of Ten-Thousands Talents Program" (No.2022R52046), the Fundamental Research Funds for the Central Universities (2021FZZX001-23), the advanced computing resources provided by the Super computing Center of Hangzhou City University, the Key R&D Program of Zhejiang (2024C01036).

## 7. REFERENCES

- [1] Seung-Mok Lee, Jongdae Jung, and Hyun Myung, "Geomagnetic field-based localization with bicubic interpolation for mobile robots," *International Journal of Control, Automation and Systems*, vol. 13, no. 4, pp. 967–977, 2015.
- [2] Igor Aleshin, Kirill Kholodkov, Ivan Malygin, Roman Shevchuk, and Roman Sidorov, "Geomagnetic survey interpolation with the machine learning approach," *arXiv preprint arXiv:2210.03379*, 2022.
- [3] Heda Zhao, Ning Zhang, Lei Xu, Penglong Lin, Yonglu Liu, and Xu Li, "Summary of research on geomagnetic navigation technology," in *IOP Conference Series: Earth and Environmental Science*, 2021.
- [4] Ulva Ria Irfan, AM Hasrianto, A Imran, A Maulana, and H Pachri, "Integrative geophysical approach for enhanced iron ore detection: Optimizing geoelectrical and geomagnetic methods," *International Journal of Design & Nature and Ecodynamics*, pp. 441–449, 2024.
- [5] Felix Goldenberg, "Geomagnetic navigation beyond the magnetic compass," in *Proceedings of IEEE/ION PLANS 2006*, 2006.
- [6] Noel Cressie, "The origins of kriging," *Mathematical geology*, vol. 22, no. 3, pp. 239–252, 1990.
- [7] George Y Lu and David W Wong, "An adaptive inverse-distance weighting spatial interpolation technique," *Computers & geosciences*, vol. 34, no. 9, pp. 1044–1055, 2008.
- [8] Martin Dietrich Buhmann, "Radial basis functions," *Acta numerica*, vol. 9, pp. 1–38, 2000.
- [9] Leroy R Alldredge, "Local functions to represent regional and local geomagnetic fields," *Geophysics*, vol. 45, no. 2, pp. 244–254, 1980.
- [10] Vincent Lesur, "Introducing localized constraints in global geomagnetic field modelling," *Earth, planets and space*, vol. 58, no. 4, pp. 477–483, 2006.
- [11] Marta Garnelo, Dan Rosenbaum, Christopher Maddison, Tiago Ramalho, David Saxton, Murray Shanahan, Yee Whye Teh, Danilo Rezende, and SM Ali Eslami, "Conditional neural processes," in *International conference on machine learning*, 2018.
- [12] Juho Lee, Yoonho Lee, Jungtaek Kim, Eunho Yang, Sung Ju Hwang, and Yee Whye Teh, "Bootstrapping neural processes," *Advances in neural information processing systems*, vol. 33, pp. 6606–6615, 2020.
- [13] Shizhe Ding, Boyang Xia, Milong Ren, and Dongbo Bu, "Niert: Accurate numerical interpolation through unifying scattered data representations using transformer encoder," *IEEE Transactions on Knowledge and Data Engineering*, vol. 36, no. 11, pp. 6731–6744, 2024.
- [14] Shizhe Ding, Boyang Xia, and Dongbo Bu, "Accurate interpolation for scattered data through hierarchical residual refinement," *Advances in Neural Information Processing Systems*, vol. 36, pp. 9144–9155, 2023.
- [15] Florinel-Alin Croitoru, Vlad Hondru, Radu Tudor Ionescu, and Mubarak Shah, "Diffusion models in vision: A survey," *IEEE transactions on pattern analysis and machine intelligence*, vol. 45, no. 9, pp. 10850–10869, 2023.
- [16] Hanqun Cao, Cheng Tan, Zhangyang Gao, Yilun Xu, Guangyong Chen, Pheng-Ann Heng, and Stan Z Li, "A survey on generative diffusion models," *IEEE transactions on knowledge and data engineering*, vol. 36, no. 7, pp. 2814–2830, 2024.
- [17] Jonathan Ho, Ajay Jain, and Pieter Abbeel, "Denoising diffusion probabilistic models," *Advances in neural information processing systems*, vol. 33, pp. 6840–6851, 2020.
- [18] Lvmin Zhang, Anyi Rao, and Maneesh Agrawala, "Adding conditional control to text-to-image diffusion models," in *Proceedings of the IEEE/CVF international conference on computer vision*, 2023.
- [19] Hyunjik Kim, Andriy Mnih, Jonathan Schwarz, Marta Garnelo, Ali Eslami, Dan Rosenbaum, Oriol Vinyals, and Yee Whye Teh, "Attentive neural processes," *arXiv preprint arXiv:1901.05761*, 2019.
- [20] Xiaoqian Chen, Zhiqiang Gong, Xiaoyu Zhao, Weien Zhou, and Wen Yao, "A machine learning modelling benchmark for temperature field reconstruction of heat-source systems," *arXiv preprint arXiv:2108.08298*, 2021.